
Accelerated Article Preview

A population of red candidate massive galaxies ~600 Myr after the Big Bang

Received: 25 July 2022

Accepted: 2 February 2023

Accelerated Article Preview

Published online: 22 February 2023

Cite this article as: Labbé, I. et al. A population of red candidate massive galaxies ~600 Myr after the Big Bang. *Nature* <https://doi.org/10.1038/s41586-023-05786-2> (2023)

Ivo Labbé, Pieter van Dokkum, Erica Nelson, Rachel Bezanson, Katherine A. Suess, Joel Leja, Gabriel Brammer, Katherine Whitaker, Elijah Mathews, Mauro Stefanon & Bingjie Wang

This is a PDF file of a peer-reviewed paper that has been accepted for publication. Although unedited, the content has been subjected to preliminary formatting. Nature is providing this early version of the typeset paper as a service to our authors and readers. The text and figures will undergo copyediting and a proof review before the paper is published in its final form. Please note that during the production process errors may be discovered which could affect the content, and all legal disclaimers apply.

1 A population of red candidate massive galaxies ~600 Myr after the Big 2 Bang

3 Ivo Labbé¹, Pieter van Dokkum², Erica Nelson³, Rachel Bezanson⁴, Katherine A. Suess^{5,6},
4 Joel Leja^{7,8,9}, Gabriel Brammer¹⁰, Katherine Whitaker^{10,11}, Elijah Mathews^{7,8,9}, Mauro
5 Stefanon^{12,13}, Bingjie Wang^{7,8,9}

6
7 ¹Centre for Astrophysics and Supercomputing, Swinburne University of Technology,
8 Melbourne, VIC 3122, Australia

9 ²Department of Astronomy, Yale University, New Haven, CT 06511, USA

10 ³Department for Astrophysical and Planetary Science, University of Colorado, Boulder, CO
11 80309, USA

12 ⁴Department of Physics and Astronomy and PITT PACC, University of Pittsburgh, Pittsburgh,
13 PA 15260, USA

14 ⁵Department of Astronomy and Astrophysics, University of California, Santa Cruz, 1156 High
15 Street, Santa Cruz, CA 95064 USA

16 ⁶Kavli Institute for Particle Astrophysics and Cosmology and Department of Physics, Stanford
17 University, Stanford, CA 94305, USA

18 ⁷Department of Astronomy & Astrophysics, The Pennsylvania State University, University
19 Park, PA 16802, USA

20 ⁸Institute for Computational & Data Sciences, The Pennsylvania State University, University
21 Park, PA, USA

22 ⁹Institute for Gravitation and the Cosmos, The Pennsylvania State University, University Park,
23 PA 16802, USA

24 ¹⁰Cosmic Dawn Center (DAWN), Niels Bohr Institute, University of Copenhagen, Jagtvej 128,
25 København N, DK-2200, Denmark

26 ¹¹ Department of Astronomy, University of Massachusetts, Amherst, MA 01003, USA

27 ¹² Departament d'Astronomia i Astrofísica, Universitat de València, C. Dr. Moliner 50, E-
28 46100 Burjassot, Valencia, Spain

29 ¹³Unidad Asociada CSIC “Grupo de Astrofísica Extragaláctica y Cosmología” (Instituto de
30 Física de Cantabria - Universitat de València)

31
32 **Galaxies with stellar masses as high as $\sim 10^{11}$ solar masses have been identified¹⁻³ out to**
33 **redshifts $z \sim 6$, approximately one billion years after the Big Bang. It has been difficult to**
34 **find massive galaxies at even earlier times, as the Balmer break region, which is needed**
35 **for accurate mass estimates, is redshifted to wavelengths beyond $2.5 \mu\text{m}$. Here we make**
36 **use of the $1\text{--}5 \mu\text{m}$ coverage of the *JWST* early release observations to search for**
37 **intrinsically red galaxies in the first ≈ 750 million years of cosmic history. In the survey**
38 **area, we find six candidate massive galaxies (stellar mass $> 10^{10}$ solar masses) at $7.4 \leq z \leq$**
39 **9.1 , $500\text{--}700$ Myr after the Big Bang, including one galaxy with a possible stellar mass of**
40 **$\sim 10^{11}$ solar masses. If verified with spectroscopy, the stellar mass density in massive**
41 **galaxies would be much higher than anticipated from previous studies based on rest-**
42 **frame ultraviolet-selected samples.**

43 The galaxies were identified in the first observations of the *JWST* Cosmic Evolution Early
44 Release Science (CEERS) program. This program obtained multi-band images at $1\text{--}5 \mu\text{m}$
45 with the Near Infrared Camera (NIRCam) in a “blank” field, chosen to overlap with existing
46 *Hubble Space Telescope* (*HST*) imaging. The total area covered by these initial data is ≈ 40
47 arcmin². The data were obtained from the MAST archive and reduced using the Grizli
48 pipeline.⁴ A catalog of sources was created, starting with detection in a deep combined

49 F277W+F356W+F444W image (see Methods for details). A total of 42,729 objects are in
50 this parent catalog.

51 We selected candidate massive galaxies at high redshifts by identifying objects that have two
52 redshifted breaks in their spectral energy distributions (SEDs), the $\lambda_{\text{rest}} = 1216 \text{ \AA}$ Lyman break
53 and the $\lambda_{\text{rest}} \sim 3600 \text{ \AA}$ Balmer break. This selection ensures that the redshift probability
54 distributions are well-constrained, have no secondary solutions at lower redshifts, and that we
55 include galaxies that have potentially high mass-to-light ratios. Specifically, we require that:
56 objects are not detected at optical wavelengths; blue in the near-infrared with $F150W -$
57 $F277W < 0.7$; red at longer wavelengths with $F277W - F444W > 1.0$; brighter than $F444W <$
58 27 AB magnitude. After visual inspection to remove obvious artefacts (such as diffraction
59 spikes), this selection produced 13 galaxies with the sought-for “double-break” spectral
60 energy distributions. Next, redshifts and stellar masses were determined with three widely-
61 used techniques, taking the contribution of strong emission lines to the rest-frame optical
62 photometry explicitly into account.^{5–15} We use the EAZY code¹⁶ (with additional strong
63 emission line templates), the Prospector- α framework¹⁷, and five configurations of the
64 Bagpipes SED-fitting code to explore systematics due to modeling assumptions. The seven
65 individual mass and redshift measurements of the 13 galaxies are listed in the Methods
66 section. We adopt fiducial masses and redshifts by taking the median value for each galaxy.
67 We note that these masses and redshifts are not definitive and that all galaxies should be
68 considered candidates.

69 As shown in Fig. 1 all 13 objects have photometric redshifts $6.5 < z < 9.1$. Six of the 13 have
70 fiducial masses $> 10^{10} M_{\odot}$ (Salpeter IMF) and multi-band images and spectral energy
71 distributions of these galaxies are shown in Figs. 2 and 3. Their photometric redshifts range
72 from $z=7.4$ to $z=9.1$. The model fits are generally excellent, and in several cases clearly
73 demonstrate that rest-frame optical emission lines contribute to the continuum emission.
74 These lines can be so strong in young galaxies that they can dominate the broad band fluxes
75 redward of the location of the Balmer break,^{6–8,14,18} and *Spitzer*/IRAC detections of optical
76 continuum breaks in galaxies at $z \gtrsim 5$ have been challenging to interpret.^{3, 5, 19–24} With *JWST*,
77 this ambiguity is largely resolved owing to the dense wavelength coverage of the NIRCam
78 filters and the inclusion of relatively narrow emission line-sensitive filter F410M,²⁵ which
79 falls within the F444W band, although the uncertainties are such that alternative solutions
80 with lower masses may exist¹⁴. The brightest galaxy in the sample, 38094, is at $z = 7.5$ and
81 may have a mass that is as high as $M \approx 1 \times 10^{11} M_{\odot}$, more massive than the present-day Milky
82 Way. It has two nearby companions with a similar break in their optical to near-IR SEDs,
83 suggesting that the galaxy may be in a group.

84 We place these results in context by comparing them to previous studies of the evolution of
85 the galaxy mass function to $z \sim 9$. These studies are based on samples that were selected in
86 the rest-frame UV using ultra-deep HST images, with *Spitzer*/IRAC photometry typically
87 acting as a constraint on the rest-frame optical SED.^{3, 15, 26–28} The bottom panel of Fig. 3
88 compares the average SED of the six candidate massive galaxies to the SEDs of *HST*-selected
89 galaxies at similar redshifts. The galaxies we report here are much redder and the differences
90 are not limited to one or two photometric bands: the entire SED is qualitatively different. This
91 is the key result of our study: we show that galaxies can be robustly identified at $z > 7$ with
92 *JWST* that are intrinsically redder than previous *HST*-selected samples at the same redshifts.
93 It is likely that these galaxies also have much higher M/L ratios, but this needs to be
94 confirmed with spectroscopy. We note that the new galaxies are very faint in the rest-frame

95 UV (median F150W~28 AB), and previous wide-field studies with HST and Spitzer²⁹ of
96 individual galaxies did not reach the required depths to find this population.

97 The masses that we derive are intriguing in the context of previous studies. No candidate
98 galaxies with $\log(M^*/M_\odot) > 10.5$ had been found before beyond $z \sim 7$, and no candidates
99 with $\log(M^*/M_\odot) > 10$ had been found beyond $z \sim 8$. Furthermore, Schechter fits to the
100 previous candidates predicted extremely low number densities of such galaxies at the highest
101 redshifts.³ This is shown by the lines in Fig. 4: the expected mass density in galaxies with
102 $\log(M^*/M_\odot) > 10$ at $z \sim 9$ was $\sim 10^2 M_\odot \text{Mpc}^{-3}$, and the *total* previously derived stellar mass
103 density, integrated over the range $8 < \log(M^*/M_\odot) < 12$, is less than $10^5 M_\odot \text{Mpc}^{-3}$. If
104 confirmed, the *JWST*-selected objects would fall in a different region of Fig. 4, in the top
105 right, as the *JWST*-derived fiducial mass densities are far higher than the expected values
106 based on the UV-selected samples. The mass in galaxies with $\log(M^*/M_\odot) > 10$ would be a
107 factor of ~ 20 higher at $z \sim 8$ and a factor of ~ 1000 higher at $z \sim 9$. The differences are even
108 greater for $\log(M^*/M_\odot) > 10.5$.

109 We infer that the possible interpretation of these *JWST*-identified “optical break galaxies”
110 falls between two extremes. If the redshifts and fiducial masses are correct, then the mass
111 density in the most massive galaxies would exceed the *total* previously estimated mass
112 density (integrated down to $M^*=10^8 M_\odot$) by a factor of ~ 2 at $z \sim 8$ and by a factor of ~ 5 at $z \sim$
113 9 . Unless the low mass samples are highly incomplete, the implication would be that most of
114 the total stellar mass at $z = 8 - 9$ resides in the most massive galaxies. Although extreme, this
115 is qualitatively consistent with the notion that the central regions of present-day massive
116 elliptical galaxies host the oldest stars in the universe (together with globular clusters), and
117 with the finding that by $z \sim 2$ the stars in the central regions of massive galaxies already
118 make up 10% – 20% of the total stellar mass density at that redshift.³⁰ A more fundamental
119 issue is that these stellar mass densities are difficult to realize in a standard LCDM
120 cosmology, as pointed out by several recent studies.^{31,32} Our fiducial mass densities push
121 against the limit set by the number of available baryons in the most massive dark matter
122 halos.

123 The other extreme interpretation is that all the fiducial masses are larger than the true masses
124 by factors of $>10-100$. We use standard techniques and multiple methods to estimate the
125 masses. Under certain assumptions for the dust attenuation law and stellar population age
126 sampling (favoring young ages with strong emission lines), low masses can be produced (see
127 Methods). This only occurs at specific redshifts ($z=5.6, 6.9, 7.7$, or about $\sim 10\%$ of the
128 redshift range of the sample) where line-dominated and continuum-dominated models
129 produce similar F410M-F444W colors. In addition, it is possible that techniques that have
130 been calibrated with lower redshift objects¹⁷ are not applicable. As an example, we do not
131 include effects of exotic emission lines or bright active galactic nuclei (AGN)¹⁴. Part the
132 sample is reported to be resolved in F200W³³ making significant contribution from AGN less
133 likely, but faint, red AGN are possible and would be highly interesting in their own right,
134 even if they could lead to changes in the masses.

135 It is perhaps most likely that the situation is in between these extremes, with some of the red
136 colours reflecting exotic effects or AGN and others reflecting high M/L ratios. Future *JWST*
137 NIRSpec spectroscopy can be used to measure accurate redshifts as well as the precise
138 contributions of emission lines and to the observed photometry. With deeper data the stellar
139 continuum emission can be detected directly for the brightest galaxies. Finally, dynamical
140 masses are needed to test the hypothesis that our description of massive halo assembly in

141 LCDM is incomplete. It may be possible to measure the required kinematics with ALMA or
142 from rotation curves with the NIRSpc IFU if the ionized gas is spatially extended.^{30,31}

- 143 1. Glazebrook, K. et al. A massive, quiescent galaxy at a redshift of 3.717. *Nature* **544**, 71–74
144 (2017)
- 145 2. Riechers, D. A. et al. Rise of the Titans: Gas Excitation and Feedback in a Binary
146 Hyperluminous Dusty Starburst Galaxy at $z \sim 6$. *Astrophys. J.* **907**, 62 (2021)
- 147 3. Stefanon, M. et al. Galaxy Stellar Mass Functions from $z \sim 10$ to $z \sim 6$ using the Deepest
148 Spitzer/Infrared Array Camera Data: No Significant Evolution in the Stellar-to-halo Mass Ratio
149 of Galaxies in the First Gigayear of Cosmic Time. *Astrophys. J.* **922**, 29 (2021)
- 150 4. Brammer, G. & Matharu, J. gbrammer/grizli: Release 2021. Zenodo (2021).
- 151 5. Schaerer, D. & de Barros, S. The impact of nebular emission on the ages of $z \approx 6$ galaxies.
152 *Astron. Astrophys.* **502**, 423–426 (2009)
- 153 6. Shim, H. et al. $z \sim 4$ H α Emitters in the Great Observatories Origins Deep Survey: Tracing
154 the Dominant Mode for Growth of Galaxies. *Astrophys. J.* **738**, 69 (2011)
- 155 7. Labbé, I. et al. The Spectral Energy Distributions of $z \sim 8$ Galaxies from the IRAC Ultra
156 Deep Fields: Emission Lines, Stellar Masses, and Specific Star Formation Rates at 650 Myr.
157 *Astrophys. J.* **777**, L19 (2013)
- 158 8. Stark, D. P. et al. Keck Spectroscopy of $3 < z < 7$ Faint Lyman Break Galaxies: The
159 Importance of Nebular Emission in Understanding the Specific Star Formation Rate and Stellar
160 Mass Density. *Astrophys. J.* **763**, 129 (2013)
- 161 9. Smit, R. et al. Evidence for Ubiquitous High-equivalent-width Nebular Emission in $z \sim 7$
162 Galaxies: Toward a Clean Measurement of the Specific Star-formation Rate Using a Sample of
163 Bright, Magnified Galaxies. *Astrophys. J.* **784**, 58 (2014)
- 164 10. Smit, R. et al. High-precision Photometric Redshifts from Spitzer/IRAC: Extreme [3.6] -
165 [4.5] Colors Identify Galaxies in the Redshift Range $z \sim 6.6 - 6.9$. *Astrophys. J.* **801**, 122 (2015)
- 166 11. Faisst, A. L. et al. A Coherent Study of Emission Lines from Broadband Photometry:
167 Specific Star Formation Rates and [O III]/H β Ratio at $3 < z < 6$. *Astrophys. J.* **821**, 122 (2016)
- 168 12. De Barros, S. et al. The GREATS H β + [O III] luminosity function and galaxy properties at
169 $z \sim 8$: walking the way of JWST. *Mon. Not. R. Astron. Soc.* **489**, 2355–2366 (2019)
- 170 13. Naidu, R. P. et al. Two remarkably luminous galaxy candidates at $Z \approx 10\text{--}12$ revealed by
171 JWST. *Astrophys. J.* **940**, L14 (2022)
- 172 14. Endsley, R., et al. A JWST/NIRCam Study of Key Contributors to Reionization: The Star-
173 forming and Ionizing Properties of UV-faint $z \sim 7\text{--}8$ Galaxies. arXiv:2208.14999 (2022)
- 174 15. Stefanon, M. et al. Blue Rest-frame UV-optical Colors in $z \sim 8$ Galaxies from GREATS: Very
175 Young Stellar Populations at 650 Myr of Cosmic Time. *Astrophys. J.* **927**, 48 (2022)
- 176 16. Brammer, G. B., van Dokkum, P. G. & Coppi, P. EAZY: A Fast, Public Photometric
177 Redshift Code. *Astrophys. J.* **686**, 1503–1513 (2008)
- 178 17. Leja, J., Johnson, B. D., Conroy, C., van Dokkum, P. G. & Byler, N. Deriving Physical
179 Properties from Broadband Photometry with Prospector: Description of the Model and a
180 Demonstration of its Accuracy Using 129 Galaxies in the Local Universe. *Astrophys. J.* **837**, 170
181 (2017)
- 182 18. Smit, R. et al. Inferred H α Flux as a Star Formation Rate Indicator at $z \sim 4\text{--}5$: Implications for
183 Dust Properties, Burstiness, and the $z = 4\text{--}8$ Star Formation Rate Functions. *Astrophys. J.* **833**,
184 254 (2016)
- 185 19. Barro, G. et al. CANDELS: The Progenitors of Compact Quiescent Galaxies at $z \sim 2$.
186 *Astrophys. J.* **765**, 104 (2013)
- 187 20. Roberts-Borsani, G., et al. Interpreting the Spitzer/IRAC colours of $7 \leq z \leq 9$ galaxies:
188 distinguishing between line emission and starlight using ALMA. *Astrophys. J.* **497**, 3440 (2020)
- 189 21. Laporte, N. et al. Probing cosmic dawn: Ages and star formation histories of candidate $z \geq 9$
190 galaxies. *Mon. Not. R. Astron. Soc.* **505**, 3336–3346 (2021)
- 191 22. Topping, M. W. et al. The ALMA REBELS Survey: Specific Star-Formation Rates in the
192 Reionization Era. arXiv e-prints arXiv:2203.07392 (2022)

- 193 23. Whitler, L. et al. Star formation histories of UV-luminous galaxies at $z \sim 6.8$: implications
194 for stellar mass assembly at early cosmic times. arXiv e-prints arXiv:2206.05315 (2022)
195 24. Hashimoto, T., et al. The onset of star formation 250 million years after the Big Bang, *Nature*
196 **557**, 392 (2018)
197 25. Roberts-Borsani, G., et al. Improving $z \sim 7$ -11 Galaxy Property Estimates with
198 JWST/NIRCam Medium-band Photometry. *Astrophys. J.* **910**, 86 (2021)
199 26. Duncan, K. et al. The mass evolution of the first galaxies: stellar mass functions and star
200 formation rates at $4 < z < 7$ in the CANDELS GOODS-South field. *Mon. Not. R. Astron. Soc.*
201 **444**, 2960–2984 (2014)
202 27. Davidzon, I. et al. The COSMOS2015 galaxy stellar mass function: Thirteen billion years of
203 stellar mass assembly in ten snapshots. *Astron. Astrophys* **605**, A70 (2017)
204 28. Song, M. et al. The Evolution of the Galaxy Stellar Mass Function at $z = 4$ -8: A Steepening
205 Low-mass-end Slope with Increasing Redshift. *Astrophys. J.* **825**, 5 (2016)
206 29. Roberts-Borsani, G. W. et al. $z \gtrsim 7$ Galaxies with Red Spitzer/IRAC [3.6]-[4.5] Colors in the
207 Full CANDELS Data Set: The Brightest-Known Galaxies at $z \sim 7$ -9 and a Probable Spectroscopic
208 Confirmation at $z = 7.48$. *Astrophys. J.* **823**, 143 (2016)
209 30. van Dokkum, P. G. et al. Dense Cores in Galaxies Out to $z = 2.5$ in SDSS, UltraVISTA, and
210 the Five 3D-HST/CANDELS Fields. *Astrophys. J.* **791**, 45 (2014)
211 31. Boylan-Kolchin, M. Stress Testing Λ CDM with High-redshift Galaxy Candidates. arXiv e-
212 prints arXiv:2208.01611 (2022)
213 32. Menci, N., et al. High-redshift Galaxies from Early JWST Observations: Constraints on Dark
214 Energy Models, *Astrophys. J.* **938**, L5
215 33. Finkelstein S., et al., CEERS Key Paper I: An Early Look into the First 500 Myr of Galaxy
216 Formation with JWST, *arXiv e-prints* arXiv:2211.05792 (2022)
217 34. van Dokkum, P., et al. Forming Compact Massive Galaxies. *Astrophys. J.* **813**, 23
218 35. Forster Schreiber, N., et al. The SINS/zC-SINF Survey of $z \sim 2$ Galaxy Kinematics:
219 SINFONI Adaptive Optics-assisted Data and Kiloparsec-scale Emission-line Properties.
220 *Astrophys. J.* **238**, 21 (2018)
221

222

223 **Figure 1: Redshifts and tentative stellar masses of double-break selected galaxies.** Shown
224 in gray circles are EAZY-determined redshifts and stellar masses using emission-line
225 enhanced templates (Salpeter IMF) for objects with $S/N > 8$ in the F444W band. Fiducial
226 redshifts and masses of the bright galaxies ($F444W < 27$ AB) that satisfy our double-break
227 selection are shown by the large red symbols. Uncertainties are the 16th -84th percentile of the
228 posterior probability distribution. All galaxies have photometric redshifts $6.5 < z < 9.1$. Six
229 galaxies are candidate massive galaxies with fiducial $M_* > 10^{10} M_{\odot}$.

230

ACCELERATED ARTICLE PREVIEW

231
232
233
234
235
236
237
238
239

Figure 2: **Images of the six galaxies with the highest apparent masses as a function of wavelength.** The fiducial stellar masses of the galaxies are $(\log(M^*/M_\odot) > 10)$. Each cutout has a size of $2.4'' \times 2.4''$. The filters range from the $0.6 \mu\text{m}$ F606W filter of *HST*/ACS to the $4.4 \mu\text{m}$ F444W *JWST*/NIRCam filter. The galaxies are undetected in the optical filters; blue in the short-wavelength NIRCam filters; and red in the long-wavelength NIRCam filters. The color stamps show F150W in blue, F277W in green, and F444W in red.

ACCELERATED ARTICLE PREVIEW

240 Figure 3: **Spectral energy distributions and stellar population model fits.** **a.** Photometry
241 (black squares), best-fitting EAZY models (red lines) and redshift probability distribution
242 $P(z)$ (gray filled histograms) of six galaxies with apparent fiducial masses $\log(M^*/M_\odot) > 10$.
243 The flux density units are f_ν . Uncertainties and upper limits (triangles) are 1σ . Fiducial best-
244 fit stellar masses and redshifts are noted. The SEDs are characterized by a double break: a
245 Lyman break and an upturn at $>3\mu\text{m}$. Emission lines are visible in the longest wavelength
246 bands in several cases. **b.** Average rest-frame SED of the 6 candidate massive galaxies (red
247 dots) and the 16th-84th percentile of the running median (shaded area). The red line is the
248 best-fit median EAZY model. Green squares and the green line show average rest-frame UV-
249 selected galaxies at $z=8,10$ from *HST+Spitzer*^{15,34}. Gray triangles show two spectroscopically
250 confirmed galaxies at $z\sim 9$ ^{23,36,44}. The double break selected galaxies are significantly redder
251 than previously identified objects at similar redshifts. This may be due to high M/L ratios or
252 effects that are not included in our modeling, such as AGN or exotic lines.
253
254
255

ACCELERATED ARTICLE PREVIEW

256
257
258
259
260
261
262
263
264
265
266

Figure 4: **Cumulative stellar mass density, if the fiducial masses of the *JWST*-selected red galaxies are confirmed.** The solid symbols show the total mass density in two redshift bins, $7 < z < 8.5$ and $8.5 < z < 10$, based on the three most massive galaxies in each bin. Uncertainties reflect Poisson statistics and cosmic variance. The dashed lines are derived from Schechter fits to UV-selected samples.³ The *JWST*-selected galaxies would greatly exceed the mass densities of massive galaxies that were expected at these redshifts based on previous studies. This indicates that these studies were highly incomplete or that the fiducial masses are overestimated by a large factor.

ACCELERATED ARTICLE PREVIEW

267

268 **Methods**

269 **Observations, reduction, and photometry**

270 This paper is based on the first imaging taken with the Near Infrared Camera (NIRCam) on
271 *JWST* as part of the Cosmic Evolution Early Release Science (CEERS) program (PI:
272 Finkelstein; PID: 1345). Four pointings have been obtained, covering ~ 38 square arcminutes
273 on the Extended Groth Strip *HST* legacy field and overlapping fully with the existing
274 HST/ACS and WFC3 footprint. NIRCam observations were taken in six broadband filters,
275 F115W, F200W, F150W, F277W, F356W, and F444W, and one medium bandwidth filter
276 F410M. The F410M medium band sits within the F444W filter and is a sensitive tracer of
277 emission lines, enabling improved photometric redshifts and stellar mass estimates of high-
278 redshift galaxies²⁹.

279 Exposures produced by Stage 2 of the *JWST* calibration pipeline (v1.5.2) were downloaded
280 from the MAST archive. The data reduction pipeline *Grism redshift and line analysis*
281 *software for space-based spectroscopy* (Grizli⁴) was used to process, align, and co-add the
282 exposures. The pipeline mitigates various artefacts, such as “snow-balls” and $1/f$ noise. The
283 To improve pixel-to-pixel variation, custom flat-field calibration images¹ were created from
284 on-sky commissioning data (program COM-1063) that are the median of the source-masked
285 and background-normalized exposures in each NIRCam detector.

286 The pipeline then subtracts a large-scale sky background, aligns the images to stars from the
287 Gaia DR3 catalog, and drizzles the images to a common pixel grid using *astrodrizzle*. The
288 mosaics are available online as part of the v3 imaging data release². Existing multi-
289 wavelength ACS and WFC3 archival imaging from *HST* were also processed with Grizli. For
290 the analysis in this paper all images are projected to a common 40 mas pixel grid. Remaining
291 background structure in the NIRCam mosaics is due to scattered light. The background is
292 generally smooth on small scales and was effectively removed with a 5” median filter after
293 masking bright sources.

294
295 We use standard *astropy*³⁶ and *photutils*³⁷ procedures to detect sources, create segmentation
296 maps, and perform photometry. The procedures are like those used in previous ground- and
297 space-based imaging surveys. Briefly, we create an inverse variance weighted combined
298 F277W + F356W + F444W image and detect sources after convolution with a Gaussian of 3
299 pixels FWHM ($0.''12$) to enhance sensitivity for point sources. PSFs were matched to the
300 F444W-band using *photutils* procedures. Photometry was performed at the locations of
301 detected sources in all filters using $0.''32$ diameter circular apertures. The fluxes were
302 corrected to total using the Kron autoscaling aperture measurement on the detection image. A
303 second small correction was applied for light outside the aperture based on the encircled
304 energy provided by the *WebbPSF* software. The final catalog contains 42,729 sources and
305 includes all available HST/ACS and *JWST*/NIRCam filters (10 bands, spanning 0.43 to 4.4
306 micron). Photometry for HST/WFC3 bands was also derived, but only used for zeropoint
307 testing as the HST/WFC3 images are several magnitudes shallower than NIRCam.

308 **Photometric zeropoints**

¹ <https://s3.amazonaws.com/grizli-v2/NircamSkyflats/flats.html>

² <https://s3.amazonaws.com/grizli-v2/JwstMosaics/v3/index.html>

310

311 The first *JWST* images were released with pre-flight zeropoints for the NIRCcam filters. The
312 pre-flight estimates do not match the in-flight performance, with errors up to $\sim 20\%$ in the
313 long wavelength (LW) bands. This analysis uses updated in-flight calibrations that were
314 provided by STScI on 7/29/2022 (jwst_0942.pmap) based on observations of two standard
315 stars. The calibrations improved the accuracy of the LW photometry but introduced errors in
316 the short wavelength (SW) bands, with variations up to 20% between detectors, as
317 determined from comparisons to previous HST/WFC3 photometry and analyses of stars in
318 the LMC and the globular cluster M92^{38,39}.

319

320 We derived new zeropoints for all SW and LW bands, for both NIRCcam modules, using two
321 independent methods. The first method (“GB”) uses zeropoints that are based on standard
322 stars observed by *JWST* in the B module and transferred to the A module using overlapping
323 stars in the LMC. The second method (“IL”) uses 5-10k galaxies at photometric redshifts 0.1
324 $< z < 5$ with $\text{SNR} > 15$ from the CEERS parent catalog and calculates the ratio between
325 observed and EAZY model fluxes for each detector, module, and photometric band. As the
326 observed wavelengths sample different rest-frame parts of the SEDs of the galaxies, errors in
327 the model fits can be separated from errors in the zeropoints. More information on the
328 methodology and the resulting zeropoints are provided on github³.

329

330 The methods agree very well, with differences of $3 \pm 3\%$ in all bands except F444W, where
331 we find a difference of 8%. We use the GB values for all bands except F444W where we take
332 the average of the GB and IL values (multiplicative corrections 1.064 for module A and
333 1.084 for module B). Using the fiducial zeropoints, Extended Data Figure 1 shows offsets
334 with respect to EAZY model fluxes, split by detector, module, and filter, showing only 0-3%
335 residuals. A third independent method used color-magnitude diagrams of stars in M92^{38,39} in
336 F090W, F150W, F277W, F444W bands, with reported consistency with the “GB” values
337 within the uncertainties. Our adopted zeropoints agree with the most recent NIRCcam flux
338 calibration (jwst_0989.pmap, Oct 2022) to within 4%. This paper adopts a 5% minimum
339 systematic error (added in quadrature) for all photometric redshift and stellar population fits
340 to account for calibration uncertainties. Finally, we compiled a sample of 450 galaxies with
341 spectroscopic redshifts $0.2 < z < 3.8$ from 3DHST⁴⁰ and MOSDEF⁴¹ to test photometric
342 redshift performance, finding a normalized median absolute deviation of $(Z_{\text{phot}} - Z_{\text{spec}})/(1 + Z_{\text{spec}})$
343 $= 2.5\%$.

344

345 **Sample selection**

346

347 The *JWST*/NIRCcam imaging in this paper reaches 5σ depths from 28.5 to 29.5 AB,
348 representing an order of magnitude increase in sensitivity and resolution beyond wavelengths
349 of $2.0 \mu\text{m}$, and allowing us for the first time to select galaxies at rest-frame optical
350 wavelengths to $z \sim 10$. To enable straightforward model-independent reproduction of the
351 sample we employ a purely empirical selection of high-redshift galaxies based on NIRCcam
352 photometry, rather than one on inferred photometric redshift or stellar mass. We select on a
353 “double break” SED: no detection in the HST ACS optical, blue in the NIRCcam SW filters,
354 and red in the NIRCcam LW filters, which is expected for sources at $z \gtrsim 7$ with Lyman-break
355 and with red UV-optical colors.

356

357 The following color selection criteria were applied:

³ <https://github.com/gbrammer/grizli/pull/107>

358 $F150W - F277W < 0.7$

359 $F277W - F444W > 1.0$

360 in addition to a non-detection requirement in HST ACS imaging

361 $SNR(B_{435}, V_{606}, I_{814}) < 2$

362 To ensure good SNR, we limit our sample to $F444W < 27$ AB magnitude and $F150W < 29$ AB

363 magnitude and require $SNR(F444W) > 8$. We manually inspected selected sources and

364 removed a small number of artefacts, such as hot pixels, diffraction spikes, and sources

365 affected by residual background issues or bright neighbors.

366

367 This selection complements the traditional “drop-out” color selection techniques based on

368 isolating the strong Lyman 1216 Å break as it moves through the filters. Drop-out selection is

369 not feasible here: the HST ACS data are not deep enough to select dropout galaxies to the

370 same equivalent limits as the NIRCcam imaging. Screening for two breaks has shown to be an

371 effective redshift selection: a similar technique was used to successfully select bright galaxies

372 at $7 < z < 9$ from wide-field HST and Spitzer data²⁹. A red $F277W-F444W$ color can be

373 produced by large amounts of reddening by dust, evolved stellar populations with a Balmer

374 Break²⁴, strong optical emission lines¹⁰, or a combination of these.

375

376 This selection produced a total of 13 sources, with a median S/N ratio in the $F444W$ band of

377 ~ 30 . The resulting sample is dark at optical wavelengths (2σ upper limit of $I_{814} > 30.4$ AB)

378 and faint in $F115W$ and $F150W$ with median ~ 28 AB magnitude, beyond the limits reached

379 with HST/WFC3 except in small areas in the Hubble Ultra Deep Field and the Frontier

380 Fields. The absence of any flux in the ACS optical, the red $I_{814} - F115W > 2.5$ and blue

381 $F115W - F150W \sim 0.3$ AB colors are consistent with a strong Lyman break moving beyond

382 the ACS I_{814} band at redshifts $z > 6$. The NIRCcam $F444W$ magnitudes are bright ~ 26 AB,

383 and the median $F150W - F444W \sim 2$ AB color is redder than any sample previously reported

384 at $z > 7^{3,18,21,29,42}$.

385

386 **Fits to the photometry**

387

388 Several methods are used to derive redshifts and stellar masses, all allowing extremely strong

389 emission lines combined with a wide range of continuum slopes: 1) *EAZY* with additional

390 templates that include strong emission lines, 2) *Prospector* with a strongly rising SFH prior

391 which favors young ages, 3) *Bagpipes* to evaluate dependence on stellar population model

392 assumptions and minimization algorithm. Finally, we also consider 4) a proposed template set

393 for high redshift galaxies with blue continua, strong emission lines, and a non-standard IMF.

394 Throughout, reported uncertainties are the 16th-84th percentile of the probability distributions.

395 A Salpeter⁴³ IMF is assumed throughout, for consistency with previous determinations of the

396 high redshift galaxy mass function^{3,28} and constraints on the IMF in the centers of the likely

397 descendants⁴⁴⁻⁴⁷. A summary of the results is presented in Extended Data Figure 3 and 4.

398

399 *I. EAZY*. The main benefits of *EAZY*⁵ are ease of use, speed, and reproducibility. *EAZY* fits

400 non-negative linear combinations of templates, with redshift and scaling of each template as

401 free parameters. The allowed redshift range was 0 – 20 and no luminosity prior was applied.

402 The standard *EAZY* template set (*tweak_fsps_QSF_12_v3*) is optimized for lower redshift

403 galaxies. High redshift stellar populations tend to be younger, less dusty, and have stronger

404 emission lines. We create a more appropriate template set by removing the oldest and dustiest

405 templates ($A_V > 2.5$) from the standard set, keeping templates 1, 2, 7, 8, 9, 10, and 11, and

406 adding two *Flexible Stellar Population Synthesis (FSPS)* templates with strong emission

407 lines. The first has a continuum that is approximately constant in F_V with $EW(H\beta+[OIII]) =$

408 650 Å, similar to NIRSspec-confirmed galaxies⁴⁸ at $z=7-8$. The second has a red continuum
409 that is constant in F_λ with $EW(H\beta+[OIII]) = 1100$ Å, comparable to line strengths inferred for
410 bright LBGs at $z=7-9$ ²⁹. Each template has an associated M/L ratio, so the template weights
411 in the fit can be converted to a total stellar mass. We fit all galaxies in the catalog with the
412 default EAZY template set first and then re-fit all galaxies at $z > 7$ using the new template
413 set. The template set is available online with the photometric catalog.⁴ The EAZY redshift
414 distribution of the sample of 13 galaxies is $7.3 < z < 9.4$, with no low-redshift interlopers
415 ($z < 6$). EAZY masses range from $9.2 < \log(M_*/M_\odot) < 10.9$.

416 *2. Prospector.* We perform a stellar population fit with more freedom than is possible in
417 EAZY using the Prospector^{17,49} framework, specifically the Prospector- α settings⁵⁰ and the
418 MIST stellar isochrones^{51,52} from Flexible Stellar Population Synthesis (FSPS)^{53,54}. This
419 mode includes non-parametric star formation histories, with a continuity prior that disfavors
420 large changes in the star formation rate between time bins.⁵⁵ It uses a two-component, age-
421 dependent dust model, allows full freedom for the gas-phase and stellar metallicity, includes
422 nebular emission where the nebulae are self-consistently powered by the stellar ionizing
423 continuum from the model.⁵⁶ The sampling was performed using the dynesty⁵⁷ nested
424 sampling algorithm. We also adopt two new priors which disfavor high-mass solutions: first,
425 a mass function prior on the stellar mass, adopting the observed $z=3$ mass function for $z > 3$
426 solutions⁵⁸, and second, a nonparametric SFH prior which favors rising SFHs in the early
427 universe and falling SFHs in the late universe, following expectations from the cosmic star
428 formation rate density. These are described in detail in Wang et al. (submitted).

429 The masses from Prospector are consistent within the uncertainties with the EAZY masses,
430 with a mean offset of $\log(M_{*Prosp}/M_{*EAZY}) = 0.1$ for objects with $> 10^{10}M_\odot$. The most massive
431 objects as indicated by EAZY are also the most massive in the Prospector fits. Prospector
432 also provides ages and star formation rates. The star formation rates are generally not very
433 well constrained in the fits, due to the lack of IR coverage. The ages are also uncertain and
434 depend strongly on the adopted prior. For a constant SFH prior Prospector finds typical ages
435 of ~ 0.3 Gyr, with substantial Balmer Breaks, whereas for strongly rising SFHs Prospector
436 finds a median mass-weighted age of 34 Myr, with strong emission lines and large amounts
437 of reddening ($A_V \sim 1.5$). This is reminiscent of the age-dust degeneracy that is well known at
438 lower redshift. Importantly, the stellar masses do not vary significantly between these two
439 priors. The red SEDs (see Figure 3) require high M/L ratios for a large range of the best-fit
440 stellar population ages, as is well known from studies of nearby galaxies⁵⁹.

441
442 *3. Bagpipes.* Fits with the Bayesian Analysis of Galaxies for Physical Inference and
443 Parameter ESTimation (Bagpipes⁶⁰) software are also considered. Compared to Prospector,
444 Bagpipes uses the Bruzual & Charlot stellar population models⁶¹ and sampling algorithm
445 Multinest⁶². While Bagpipes does not cover new parameter space compared to Prospector, it
446 allows us to evaluate how sensitive the masses are to the adopted stellar population model or
447 fitting technique. Furthermore, Bagpipes is relatively fast, so we can use it explore the effect
448 of modeling assumptions to investigate the role of systematic uncertainties on the derived
449 redshift and stellar mass. We focus on attenuation law, SFH, age sampling priors, and SNR.

450
451 *A. bagpipes_csf_salim:* baseline model of constant SFH with redshift 0 to 20, age_max from
452 1 Myr to 10 Gyr, metallicity between 0.01 and 2.5 Solar, ionization parameter $-4 < \log(U) < -$
453 2, a Salim⁶³ attenuation $0 < A_V < 4$, and adopting a linear prior in age and log prior in

⁴ <https://github.com/ivolabbe/red-massive-candidates>

454 metallicity and ionization and uniform prior in redshift, age, and A_V . The Salim law varies
455 between a steep SMC-like extinction law at low optical depth and a flat Calzetti-like dust law
456 at large optical depth, in accordance with empirical studies⁶³ and theoretical expectations⁶⁴.
457 The Bagpipes masses and redshifts are similar on average to those of EAZY and Prospector,
458 with a mean offset of $\log(M^*/M^*_{\text{EAZY}}) = 0.0$ for the massive sample.

459
460 *B. Bagpipes_rising_salim*: this model is not intended to search for best fit in a wide
461 parameter space but only in a restricted space to increase the emission line contribution to the
462 reddest filter, F444W, and decrease the stellar masses. The model is restricted to rising star
463 formation rates at high redshift (delayed $\tau > 0.5$ Gyr) and redshifts to $z < 9.0$ to force the
464 Hb+[OIII] complex to fall within the F444W filter. The fits show strong emission lines, low
465 ages (median ~ 30 Myr) and high dust content (median $A_V \sim 1.7$). Even with these
466 restrictions, the mean stellar mass agrees well with the baseline (mean $\log(M^*/M^*_A) = -0.1$
467 for objects with $> 10^{10} M_\odot$).

468
469 *C. Bagpipes_csf_salim_logage*: like model (A) but with a logarithmic age prior, which is
470 heavily weighted towards very young ages. For the 5 reddest, most massive galaxies in A the
471 results are unchanged, whereas 6 other galaxies are now placed at significantly lower masses
472 (inconsistent with model A, given the uncertainties), including 14924 (from $\log(M^*/M_\odot) =$
473 10.1 to 8.7). The $P(z)$ of these lower mass solutions is remarkably narrow and clustered in
474 narrow spikes at $z = 5.6, 6.9, 7.7$, where the F410M filter cannot distinguish between strong
475 lines and continuum SEDs (see Extended Data Figure 5 and 6).

476
477 *D. Bagpipes_csf_salim_logage_snr10*: to test if the fit in (C) is driven by the high SNR in
478 long wavelength filters (which put all the weight in the fits there), we impose an error floor of
479 10% on the photometry which approximately balances the SNR across all NIRCcam bands.
480 Since JWST is still in early days of calibration, some limit on SNR is prudent. The SNR-
481 limited fits result in high mass solutions for 11/13 galaxies. Notably, the uncertainties on the
482 stellar mass do not encompass the low mass solution from (C) indicating that detailed
483 assumptions on the treatment of SNR can introduce systematic changes.

484
485 *E. Bagpipes_csf_smc_logage*: SMC-extinction is often used in modeling high-redshift
486 galaxies¹⁴. Our Bagpipes modeling use Salim-type dust which includes the SMC-like
487 extinction at low optical depth, but it is useful to evaluate fits that are restricted to a steep
488 extinction law in combination with a logarithmic age prior favoring young ages. The results
489 are remarkably different from any of the modeling above: 10/13 galaxies show very low
490 stellar masses (in the range $10^8 M_\odot$ - $10^9 M_\odot$) in combination with extremely young ages (1-5
491 Myr). Another notable aspect is that these fits do not match the blue part of the SED well
492 (NIRCcam SW F115W, F150W, F200W) and the fits appear driven by the high SNR in the
493 NIRCcam LW filters (see Extended Data Figure 3). Most fits have significantly worse χ^2 than
494 the high-mass fits (Eazy, Prospector, Bagpipes A-D).

495
496 In conclusion, the derived masses depend on assumed attenuation law, parameterization of
497 ages, and treatment of photometric uncertainties. Together, these aspects can produce lower
498 redshifts and lower masses by up to factors of 100 in ways that are not reflected by the
499 random uncertainties. Therefore, different assumptions can change the stellar masses and
500 redshifts systematically and the uncertainties are likely underestimated.

501
502 While neither high, nor low-mass models can be excluded with the currently available data,
503 there are two features that would suggest the ultra-young, low-mass solutions are less

504 plausible. First, while 1-5 Myr ages are formally allowed, the galaxy would not be causally-
505 connected – $10^{8.5}M_{\odot}$ of star formation would have started spontaneously on timescales less
506 than a dynamical time (although dynamical times are uncertain until velocity dispersions and
507 corresponding sizes are measured). In addition, the probability of catching most galaxies at
508 that precise moment is low - given the ~ 200 Myr search window at $z=7-9$. It would suggest
509 there are >40 older and more massive galaxies for every galaxy in our sample.

510
511 Second, the $P(z)$ of the low-mass solutions are extremely narrow and concentrated at nearly
512 discrete redshifts $z=5.6, 6.9, 7.7$ (e.g. 38094 $z=6.93 \pm 0.01$). Here strong H α and H β + $[\text{OIII}]$
513 transition between the overlapping F356W, F410M, and F444W filter edges (see Extended
514 Data Figure 5). A single line can contribute to several bands (e.g., $[\text{OIII}]5007$ at $z=6.9$), with
515 great flexibility due to the rapidly varying transmission at the filter edges. The result is that
516 line and continuum dominated models are degenerate due to undersampling of the SED and
517 resulting aliasing, but only at specific redshifts.

518
519 While finding one 5 Myr galaxy exactly in this narrow window could be luck, we find that
520 10/13 galaxies can only be fit with low mass, ultra-young models at these discrete redshifts
521 $z=5.6, 6.9, 7.7$. Such an age and $P(z)$ distribution for the sample, at precisely the redshifts
522 where this fortuitous overlap between filters occurs ($\sim < 8\%$ of the redshift range between
523 $z=5-9$), is not implausible. To rule out that the spiked nature of the $P(z)$ is the result of our
524 double break selection, we perform simple simulations. We take random draws from the
525 posteriors of line-dominated model E, redshift the models to a uniform distribution between 4
526 and 10, perturb with the observational errors, and apply our double break selection criterion
527 to the simulated photometry (see Extended Data Figure 6). This suggests that even if the
528 sample were line-dominated with ages < 5 Myr, the redshift distribution should be different
529 (not spiked) suggesting that these fits suffer from aliasing. In contrast, $P(z)$ of high-mass
530 model B is broadly self-consistent with the selection function based on the model B fits.
531 The likely reason that this effect primarily occurs with an SMC extinction law is because of
532 the strong wavelength dependence (steep in the FUV, flatter in optical). For the sample in this
533 paper, fits with SMC have difficulty reproducing the overall (rest-optical) red SED shape.
534 This can be clearly seen in Extended Data Figure 3, where the SMC based fits have strongly
535 “curved” continuum, which are generally too steep in the rest-UV and too flat in the rest-
536 optical (F356W, F410W, F444W bands), requiring strong emission lines at specific redshifts
537 to produce the red colors.

538
539 *5. FSPS-hot model.* For completeness we also consider recently proposed “*fsps-hot*”
540 models⁶⁵, which consist of templates with blue continua, strong emission lines, and with a
541 modified extremely bottom-light IMF which produces lower masses. Such an IMF is
542 proposed to be appropriate for the extreme conditions that might be expected in high redshift
543 galaxies. For 10 of 13 galaxies (including all massive $> 10^{10}M_{\odot}$ sources), the *fsps-hot*
544 template set provides poorer fits to the photometry than the *fsps-wulturecorn* set (median $\Delta\chi^2$
545 = 31), due to the lack of red templates. The *fsps-hot* set places 9/13 galaxies in a narrow
546 redshift range $z=7.7$ with very small uncertainties $\sigma(z) = 0.05$, reminiscent of the spiked
547 distribution found earlier for Bagpipes model E. The blue template set can only produce red
548 colors if strong emission lines are placed at specific redshifts. Since the fits are overall poor
549 and no additional insight is gained, we do not consider these masses further to avoid
550 confusion due to adopting vastly different IMFs. The extremely bottom-light IMF, with
551 suppression of (invisible) low mass stars, is untestable with photometric data.

552
553

Fiducial redshifts and stellar masses

554

555 The majority of methods explored produce good fits and consistent masses and redshifts.
556 Rather than favor one method over the others we derive “fiducial” masses and redshifts for
557 each object by taking the median values of the EAZY (1), Prospector (2), the 5 Bagpipes fits
558 (3-7) results of each galaxy. As discussed in the main text, the consistency between various
559 methods may largely indicate a consistency in underlying assumptions. Different assumptions
560 can change the stellar masses and redshifts systematically in ways that are not reflected by
561 the random uncertainties.

562

563 Additionally, we do not consider contributions from exotic emission line species nor include
564 AGN templates in the fits¹⁴. All objects in this paper should be considered candidate massive
565 galaxies, to be confirmed with spectroscopy.

566

567 **Lensing**

568

569 A potential concern is that the fluxes (and therefore the masses) of some or all the galaxies
570 are boosted by gravitational lensing. No galaxy is close to the expected Einstein radius of
571 another object. The bright galaxy that is 1.2” to the southwest of 38094 has $z_{\text{grism}} \approx 1.15$ and
572 $M^* \approx 10.63$ (object number 28717 in 3D-HST AEGIS catalog²³), and an Einstein radius (\sim
573 0.4”) that is $0.3\times$ the distance to 38094. If we assume that the mass profile of the lensing
574 galaxy is an isothermal sphere, then the magnification is $1/(1 - \theta_E/\theta)$ where θ is the
575 separation from the foreground source and θ_E is the Einstein radius. This would imply a
576 relatively modest -0.15 dex correction to the stellar mass. We apply this correction when
577 calculating densities in Figure 4.

578

579 **Volume**

580

581 Stellar mass densities for galaxies with $M^* > 10^{10} M_{\odot}$ are calculated by grouping the galaxies
582 in two broad redshift bins ($7 < z < 8.5$ and $8.5 < z < 10$). At $z \sim 8.5$ the Lyman Break moves
583 through the F115W filter, allowing galaxies to be separated into the two bins. The cosmic
584 volume is estimated by integrating between the redshift limits over 38 sq arcmin, making no
585 corrections for contamination or incompleteness. The key result is driven by the most
586 massive galaxies. Any incompleteness would increase the derived stellar mass densities,
587 while contamination would decrease it. Cosmic variance is about 30%, calculated using a
588 web calculator^{66,5}. The error bars on the densities are the quadratic sum of the Poisson
589 uncertainty and cosmic variance, with the Poisson error dominant. The volume estimate is
590 obviously simplistic, but the color selection function (see Extended Data Figure 6) suggests
591 that most of the sample should lie between $7 < z < 10$. A more refined treatment does not
592 seem warranted given that the main (orders of magnitude) uncertainty in our study is the
593 interpretation of the red colors of the galaxies.

594

595 **Data Availability.** The HST data are available in the Mikulski Archive for Space Telescopes
596 (MAST; <http://archive.stsci.edu>), under program ID 1345. Photometry, EAZY template set,
597 fiducial redshifts, and stellar masses of the sources presented here are available at
598 <https://github.com/ivolabbe/red-massive-candidates>.

599

600 **Code Availability.** Publicly available codes and standard data reduction tools in the Python
601 environments were used: Grizli,⁴ EAZY⁵, astropy⁶⁴, photutils⁶⁵, Prospector^{17,37,38}.

602 **Acknowledgements.** We are grateful to the CEERS team for providing these exquisite public
603 JWST data so early in the mission. We thank Michael Boylan-Kolchin for helpful discussions
604 on the theoretical context of this work. Cloud-based data processing and file storage for this
605 work is provided by the AWS Cloud Credits for Research program. The Cosmic Dawn
606 Center is funded by the Danish National Research Foundation. K.W. wishes to acknowledge
607 funding from Alfred P. Sloan Foundation Grant FG-2019-12514. M.S. acknowledges project
608 PID2019-109592GB-I00/AEI/10.13039/501100011033 from the Spanish Ministerio de
609 Ciencia e Innovacion - Agencia Estatal de Investigacion.

610 **Author Contributions.** I.L. performed the photometry, devised the selection method, and led
611 the analysis. P.v.D. drafted the main text. I.L. wrote the Methods section and produced the
612 figures. G.B. developed the image processing pipeline and created the image mosaics. E.N.
613 and R.B. identified the first double break galaxy, prompting the systematic search for these
614 objects. J.L., B.W., K.S., and E.M. ran the Prospector analysis. All authors contributed to the
615 manuscript and aided the analysis and interpretation.

616
617 **Author Information.** The authors declare that they have no competing financial interests.
618 Correspondence and requests for materials should be addressed to I.L. (email:
619 ilabbe@swin.edu.au).

- 620
621
622 36. Astropy Collaboration. The Astropy Project: Sustaining and Growing a Community-oriented
623 Open-source Project and the Latest Major Release (v5.0) of the Core Package, *Astrophys. J.* **935**,
624 167 (2022)
625 37. Bradley L., *et al.* astropy/photutils: 1.5.0. (2022) doi:10.5281/zenodo.6825092
626 38. Boyer, M.-L., Anderson, J., Gennaro, M., *et al.* The JWST Resolved Stellar Populations
627 Early Release Science Program I.: NIRCam Flux Calibration. *arXiv e-prints* arXiv:2209.03348
628 (2022)
629 39. Nardiello D., *et al.* Photometry and astrometry with JWST -- I. NIRCam Point Spread
630 Functions and the first JWST colour-magnitude diagrams of a globular cluster. *arXiv e-prints*
631 arXiv:2209.06547 (2022)
632 40. Skelton, R. E. *et al.* 3D-HST WFC3-selected Photometric Catalogs in the Five
633 CANDELS/3D-HST Fields: Photometry, Photometric Redshifts, and Stellar Masses. *Astrophys.*
634 *J.S* **214**, 24 (2014)
635 41. Kriek, M. *et al.* The MOSFIRE Deep Evolution Field (MOSDEF) Survey: Rest-frame
636 Optical Spectroscopy for ~1500 H- selected Galaxies at $1.37 < z < 3.8$. *Astrophys. J.S* **218**, 15
637 (2015)
638 42. Zitrin, A., *et al.* Lyman- α Emission from a Luminous $z = 8.68$ Galaxy: Implications for
639 Galaxies as Tracers of Cosmic Reionization. *Astrophys. J.* **810**, L12 (2015)
640 43. Salpeter, E. The Luminosity Function and Stellar Evolution. *Astrophys. J.* **121**, p.161
641 44. Treu T., *et al.* The Initial Mass Function of Early-Type Galaxies. *Astrophys. J.* **709**, 2 (2010)
642 45. Cappellari M., *et al.* Systematic variation of the stellar initial mass function in early-type
643 galaxies, *Nature* **544**, 485-488 (2012)
644 46. Conroy C. & van Dokkum P. The Stellar Initial Mass Function in Early-type Galaxies From
645 Absorption Line Spectroscopy. II. Results, *Astrophys. J.* **760**, 71 (2012)
646 47. van Dokkum P., *et al.* The Stellar Initial Mass Function in Early-type Galaxies from
647 Absorption Line Spectroscopy. III. Radial Gradients. *Astrophys. J.* **841**, 68 (2017)
648 48. Schaerer D., *et al.* First look with JWST spectroscopy: Resemblance among $z \sim 8$ galaxies
649 and local analogs. *Astron. Astrophys.* **665**, L4 (2022)
650 49. Johnson, B. D., Leja, J., Conroy, C. & Speagle, J. S. Stellar Population Inference with
651 Prospector. *Astrophys. J.S* **254**, 22 (2021)
652 50. Leja, J. *et al.* An Older, More Quiescent Universe from Panchromatic SED Fitting of the 3D-
653 HST Survey. *Astrophys. J.* **877**, 140 (2019)

- 654 51. Choi, J. et al. Mesa Isochrones and Stellar Tracks (MIST). I. Solar-scaled Models.
655 *Astrophys. J.* **823**, 102 (2016)
- 656 52. Dotter, A. MESA Isochrones and Stellar Tracks (MIST) 0: Methods for the Construction of
657 Stellar Isochrones. *Astrophys. J. S* **222**, 8 (2016)
- 658 53. Conroy, C., Gunn, J. E., White, M. The Propagation of Uncertainties in Stellar Population
659 Synthesis Modeling. I. The Relevance of Uncertain Aspects of Stellar Evolution and the Initial
660 Mass Function to the Derived Physical Properties of Galaxies. *Astrophys. J.* **699**, 486 (2009)
- 661 54. Conroy, C., Gunn, J. E. The Propagation of Uncertainties in Stellar Population Synthesis
662 Modeling. III. Model Calibration, Comparison, and Evaluation. *Astrophys. J.* **712** 833 (2010)
- 663 55. Leja, J., Carnall, A. C., Johnson, B. D., Conroy, C. & Speagle, J. S. How to Measure Galaxy
664 Star Formation Histories. II. Nonparametric Models. *Astrophys. J.* **876**, 3 (2019)
- 665 56. Byler, N., Dalcanton, J. J., Conroy, C. & Johnson, B. D. Nebular Continuum and Line
666 Emission in Stellar Population Synthesis Models. *Astrophys. J.* **840**, 44 (2017)
- 667 57. Speagle J. DYNESTY: a dynamic nested sampling package for estimating Bayesian
668 posteriors and evidences. *Mon. Not. R. Astron. Soc.* 493, 3132-3158 (2020)
- 669 58. Leja, J., et al. A New Census of the $0.2 < z < 3.0$ Universe. I. The Stellar Mass Function.
670 *Astrophys. J.* **893**, 111 (2020)
- 671 59. Bell E. & de Jong R., Stellar Mass-to-Light Ratios and the Tully-Fisher Relation. *Astrophys.*
672 *J.* 550, 1 (2001)
- 673 60. Carnall, A., et al. Inferring the star formation histories of massive quiescent galaxies with
674 BAGPIPES: evidence for multiple quenching mechanisms. *Mon. Not. R. Astron. Soc.* **480**, 4,
675 4379-4401 (2018)
- 676 61. Bruzual, G. & Charlot, S. Stellar population synthesis at the resolution of 2003. *Mon. Not. R.*
677 *Astron. Soc.* **344**, 1000-1028 (2003)
- 678 62. Feroz, F., et al. Importance Nested Sampling and the MultiNest Algorithm, *Open J. of*
679 *Astrophys.* **2**, 10 (2019)
- 680 63. Salim, S., Boquien, M., Lee, J. C., Dust Attenuation Curves in the Local Universe:
681 Demographics and New Laws for Star-forming Galaxies and High-redshift Analogs. *Astrophys.*
682 *J.* **859** (2018)
- 683 64. Chevallard, J., et al., Insights into the content and spatial distribution of dust from the
684 integrated spectral properties of galaxies, *Mon. Not. R. Astron. Soc.* **432**, 2061 (2013)
- 685 65. Steinhardt, C. L., et al. Templates for Fitting Photometry of Ultra-High-Redshift Galaxies
686 *arXiv e-prints* arXiv:2208.07879 (2022)
- 687 66. Trenti, M. & Stiavelli, M. Cosmic Variance and Its Effect on the Luminosity Function
688 Determination in Deep High-z Surveys, *Astrophys. J.* **676**, 767-780 (2008)
- 689
690
691
692
693

694 **Extended Data**

695

696

697 Extended Data Figure 1. **Systematic offsets in photometry as a function of wavelength.**

698 The offsets are estimated by the ratio of the observed fluxes to the EAZY best-fit model

699 fluxes for 5,000-10,000 sources at $0.1 < z < 5$ in the CEERS field. The offsets are calculated

700 separately for each detector (1-4), module (A/B), and filter. Symbols are slightly spread out

701 in wavelength for clarity. **a.** The first in-flight NIRCam flux calibration update of 29 July

702 2022 (jwst_0942.pmap) introduced significant offsets in NIRCam short-wavelength

703 zeropoints. **b.** After adopting our fiducial zeropoints, residual offsets are $\sim < 3\%$ across all

704 bands. This paper adopts a 5% minimum systematic error for all photometric redshift and

705 stellar population fits.

706

ACCELERATED ARTICLE PREVIEW

707
708
709
710
711
712
713
714
715
716
717
718
719
720
721
722
723
724
725
726
727

Extended Data Figure 2. **Images of the seven galaxies with apparent lowest mass.** The galaxies satisfy the color-color selection and have fiducial masses $\log(M_*/M_\odot) < 10$. The layout and panels of the figure are identical to Fig. 2 in the main text. Each cutout has a size of $2.4'' \times 2.4''$. The filters range from the $0.6 \mu\text{m}$ F606W filter of HST/ACS to the $4.4 \mu\text{m}$ F444W JWST/NIRCam filter.

ACCELERATED ARTICLE PREVIEW

728 Extended Data Figure 3: **Spectral energy distributions of all 13 galaxies that satisfy the**
729 **color-color selection. a.** The layout of the figure is identical to Fig. 3a in the main text. In
730 addition, an alternative model fit (model E, see Methods) is shown that produces low stellar
731 masses (blue), but generally requires extremely young ages (<5 Myr) at specific narrow
732 redshift intervals. **b.** The panel at the lower right shows the averaged rest-frame SED of the
733 seven galaxies with fiducial $\log(M^*/M_\odot) < 10$, compared to previously-found galaxies at
734 similar redshifts (see Fig. 3).
735
736

ACCELERATED ARTICLE PREVIEW

737
738
739
740
741
742
743

Extended Data Figure 4: **Results of the stellar population fitting.** Masses (**a**), redshifts (**b**), and the chi-squared fit quality (**c**) of the 13 galaxies that satisfy the color-color selection. For each galaxy seven different measurements are shown, as well as the median of the seven that is adopt as the fiducial value (see Methods section). These medians are listed in Extended Data Table 2.

ACCELERATED ARTICLE PREVIEW

744
745
746
747
748
749
750
751
752
753
754
755
756
757
758
759
760
761
762
763
764
765
766
767
768
769
770
771
772
773
774
775
776
777

Extended Data Figure 5. **Color difference between emission line and continuum-dominated models.** The line-dominated model is a 5 Myr old constant SFH with nebular emission lines. The continuum dominated model is a 50 Myr old CSF without emission lines. Two colors differences involving the line-sensitive F410M filter are shown: F356W-F410M (green) and F410M-F444W (red) and the sum of their absolute values. When H α and H β +[OIII] move through the filters with redshift, the emission line sensitive medium-band F410M filter produces a strong signature, except at $z=5.6, 6.9, 7.7$, where the lines transition between filters. Here continuum and line-dominated SEDs produce similar colors due to undersampling of the SED by the filters.

ACCELERATED ARTICLES PREVIEW

778
779
780
781
782
783
784
785
786
787
788
789
790
791
792

Extended Data Figure 6. **Stacked redshift probability distribution of all 13 galaxies in the sample.** The $P(z)$ were derived using Bagpipes (as described in Methods). Redshifts of a high mass solution are shown in red (model B: Salim dust attenuation law, rising SFH, linear age prior, continuum dominated) and a low mass solution are shown in blue (model E: SMC dust, logarithmic age prior, emission line dominated). Other high mass fits (e.g., Prospector, EAZY) and low mass fits produce similar $P(z)$. Solid curves show expected selection function under the assumption of continuum (red) or line-dominated models (blue). The high-mass continuum-dominated $P(z)$ broadly traces the expected selection functions. The low-mass line-dominated $P(z)$ is not expected for selection of a line-dominated model. The $P(z)$ is concentrated at narrow redshifts around $z=5.6, 6.9, 7.7$ (black dotted lines) where the line-sensitive F410M cannot distinguish between continuum and strong lines due to aliasing.

ACCELERATED ARTICLE PREVIEW

793

794

795

796

797

798 Extended Data Table 1. **HST/ACS and JWST/NIRCam Photometry of the double break**

799 **sample**. Units are nJy. A fixed 5% uncertainty is added in quadrature to the photometric

800 uncertainties account for calibration errors before fitting with EAZY, Prospector, and

801 Bagpipes.

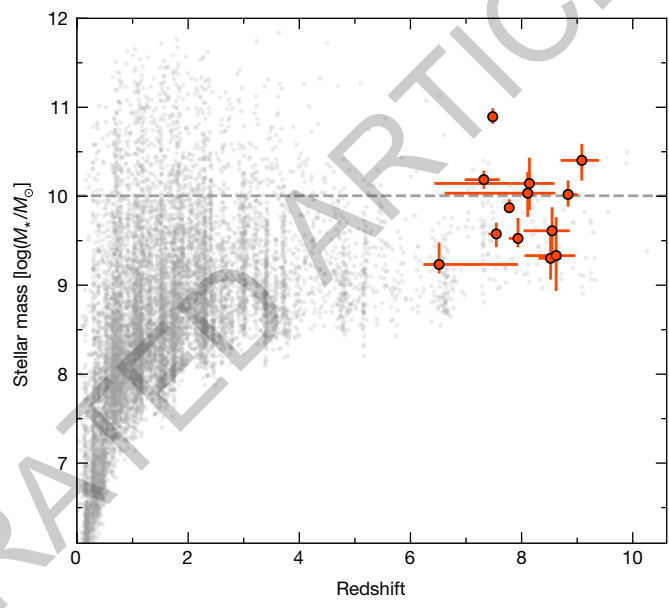
802

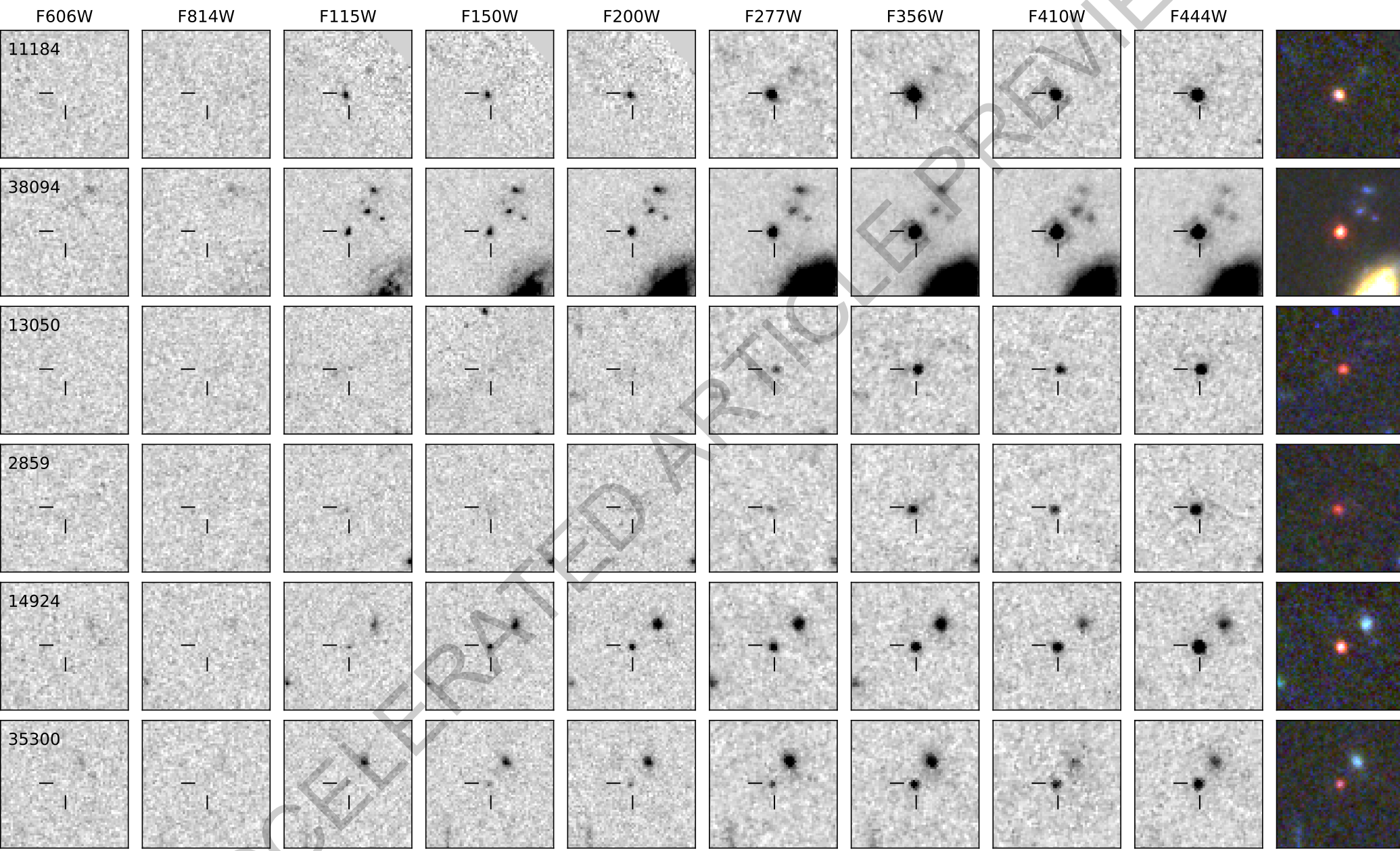
ACCELERATED ARTICLE PREVIEW

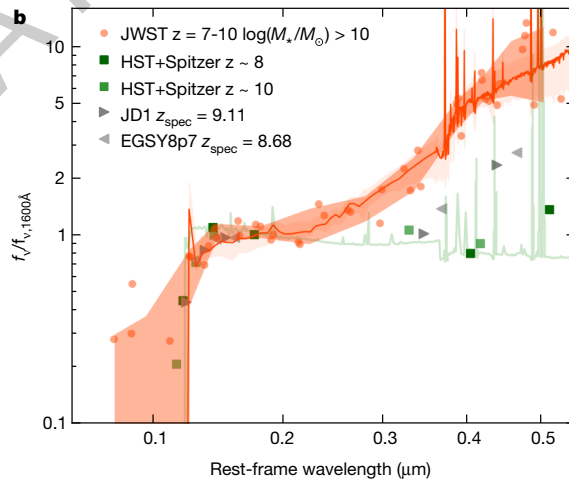
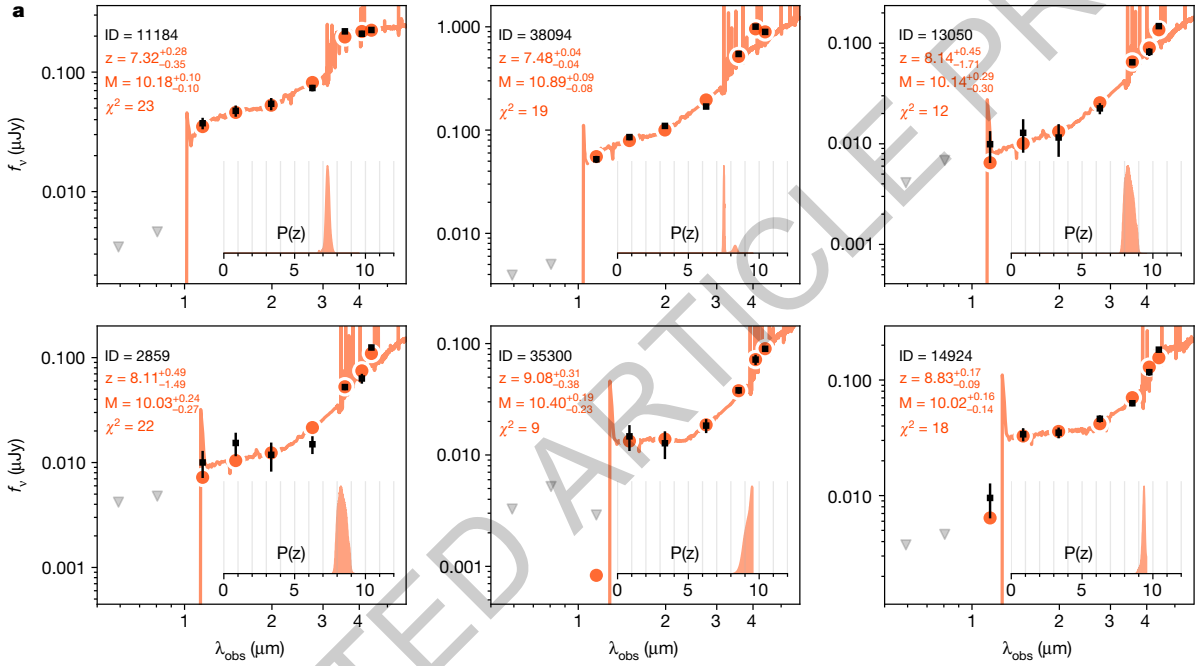
803
804
805
806
807
808
809
810
811
812

Extended Data Table 2. **Fiducial redshifts and stellar masses of the double break sample.**
The adopted redshift and stellar mass are the medians of redshifts and masses computed with 7 different methods (EAZY, Prospector, and Bagpipes (5 variations, including dust, SFH, age prior, and SNR limit), see Methods. A Salpeter IMF is assumed. Two uncertainties are listed ($\pm(\text{ran}) \pm (\text{sys})$) with random uncertainties (ran) corresponding to the median 16th and 84th percentile of the combined posterior distributions, and systematic uncertainties (sys) corresponding to the extremes of all model fits.

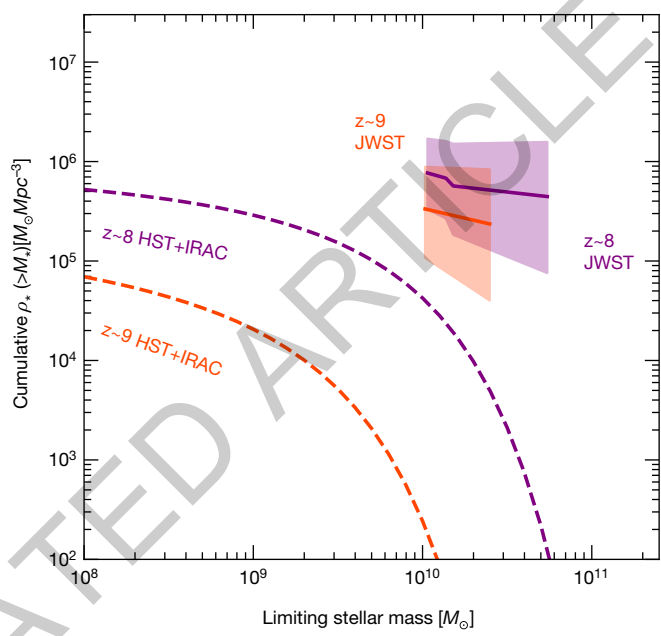
ACCELERATED ARTICLE PREVIEW

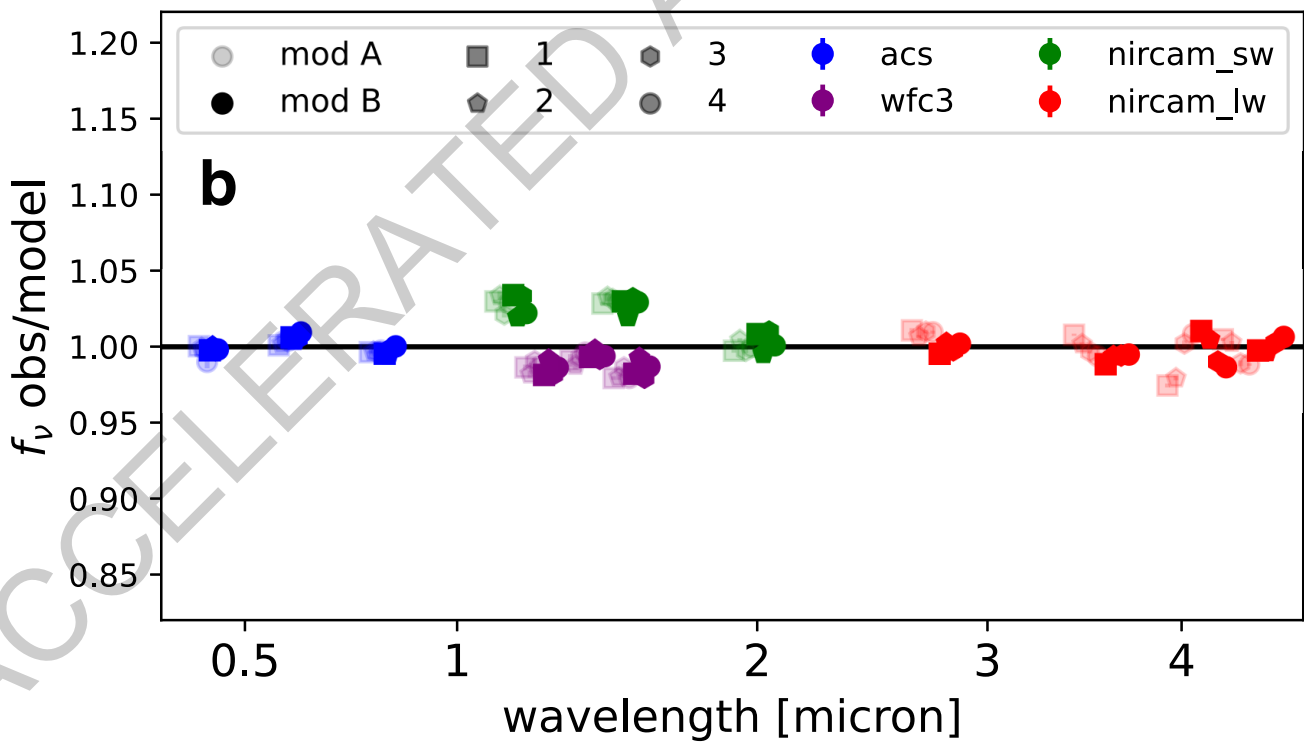
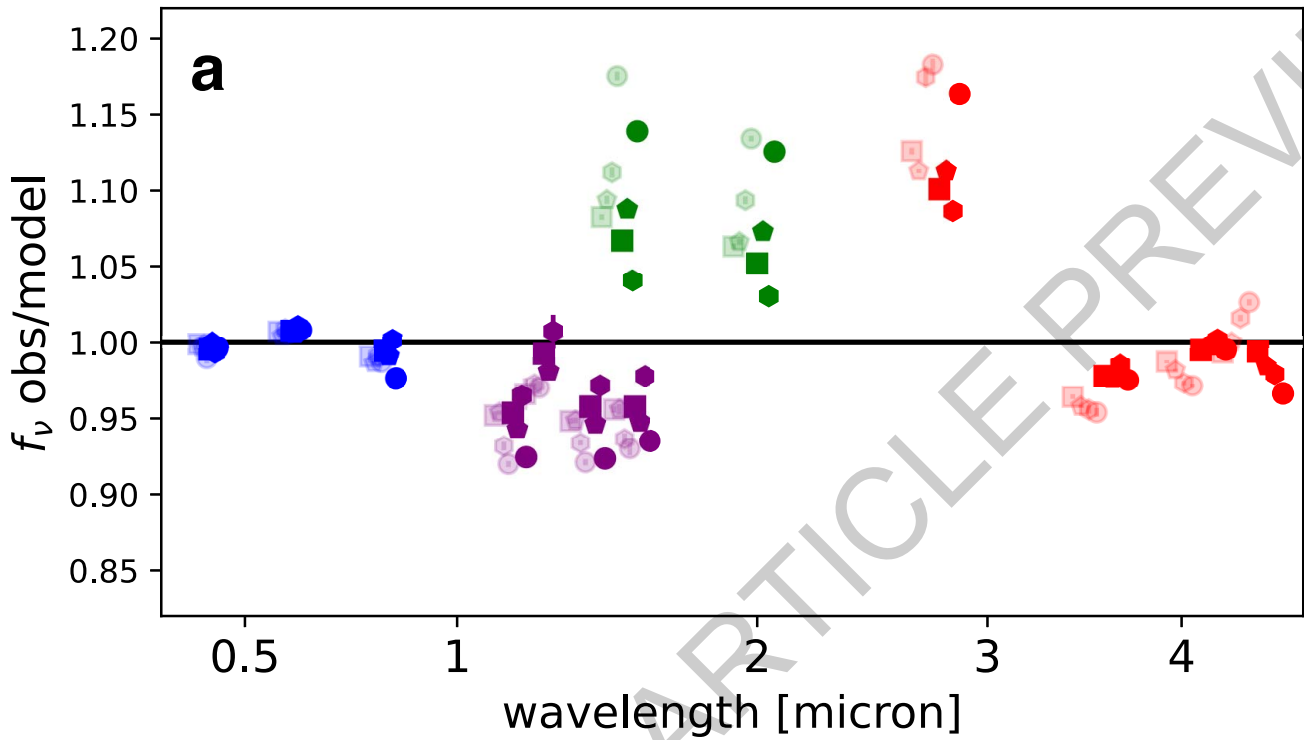




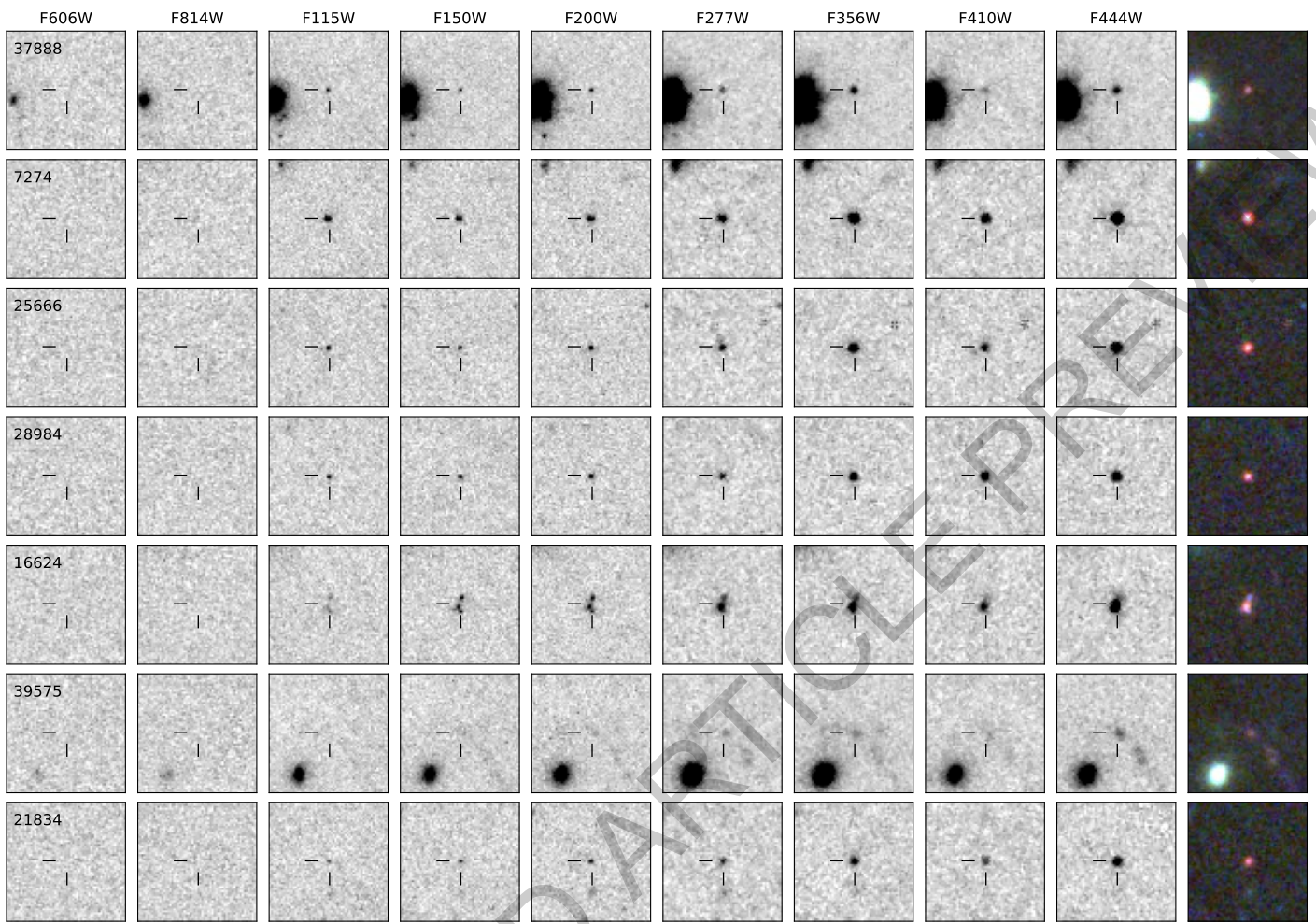


ACCELERATED ARTICLE PREVIEW



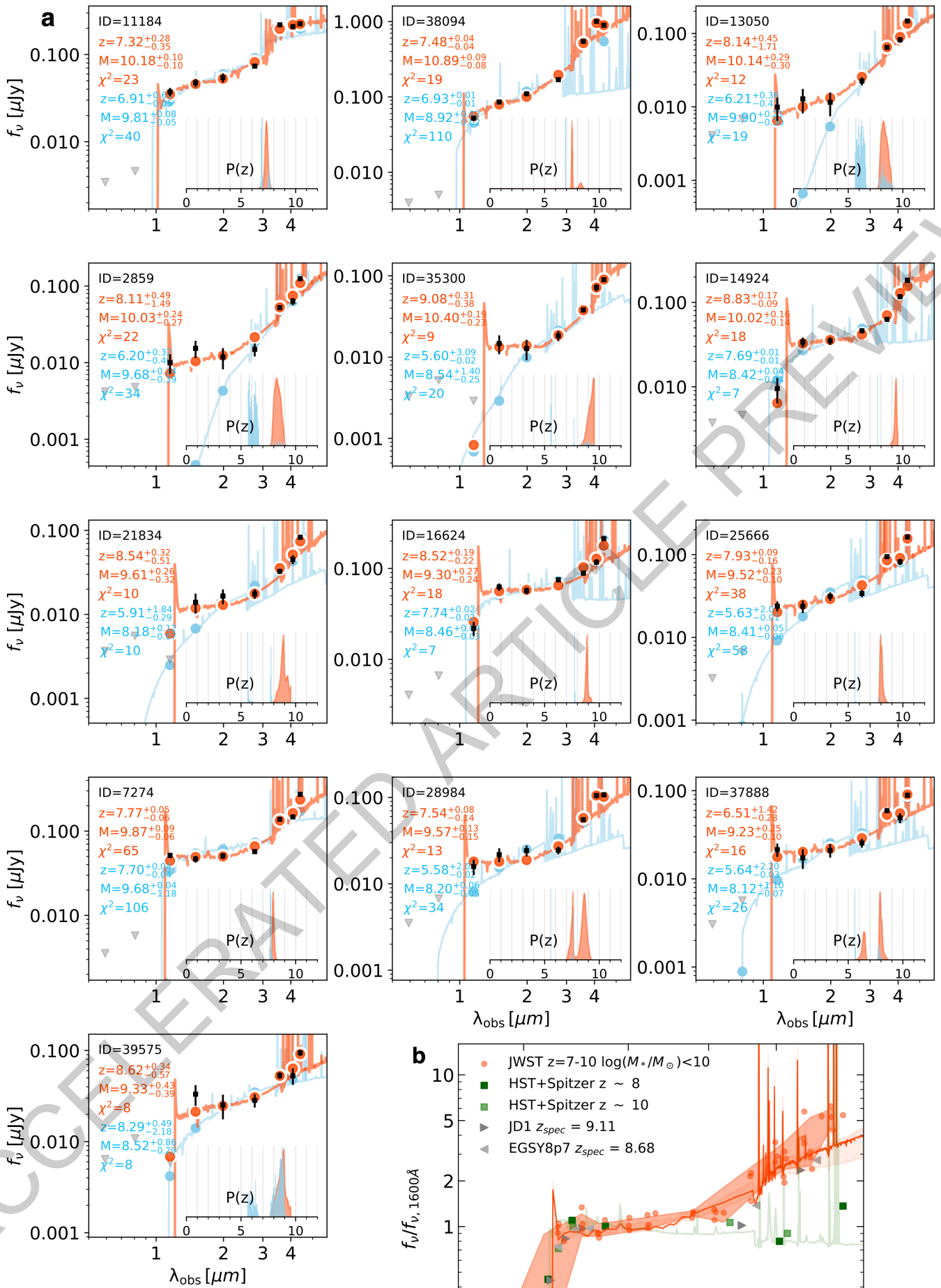


Extended Data Fig. 1

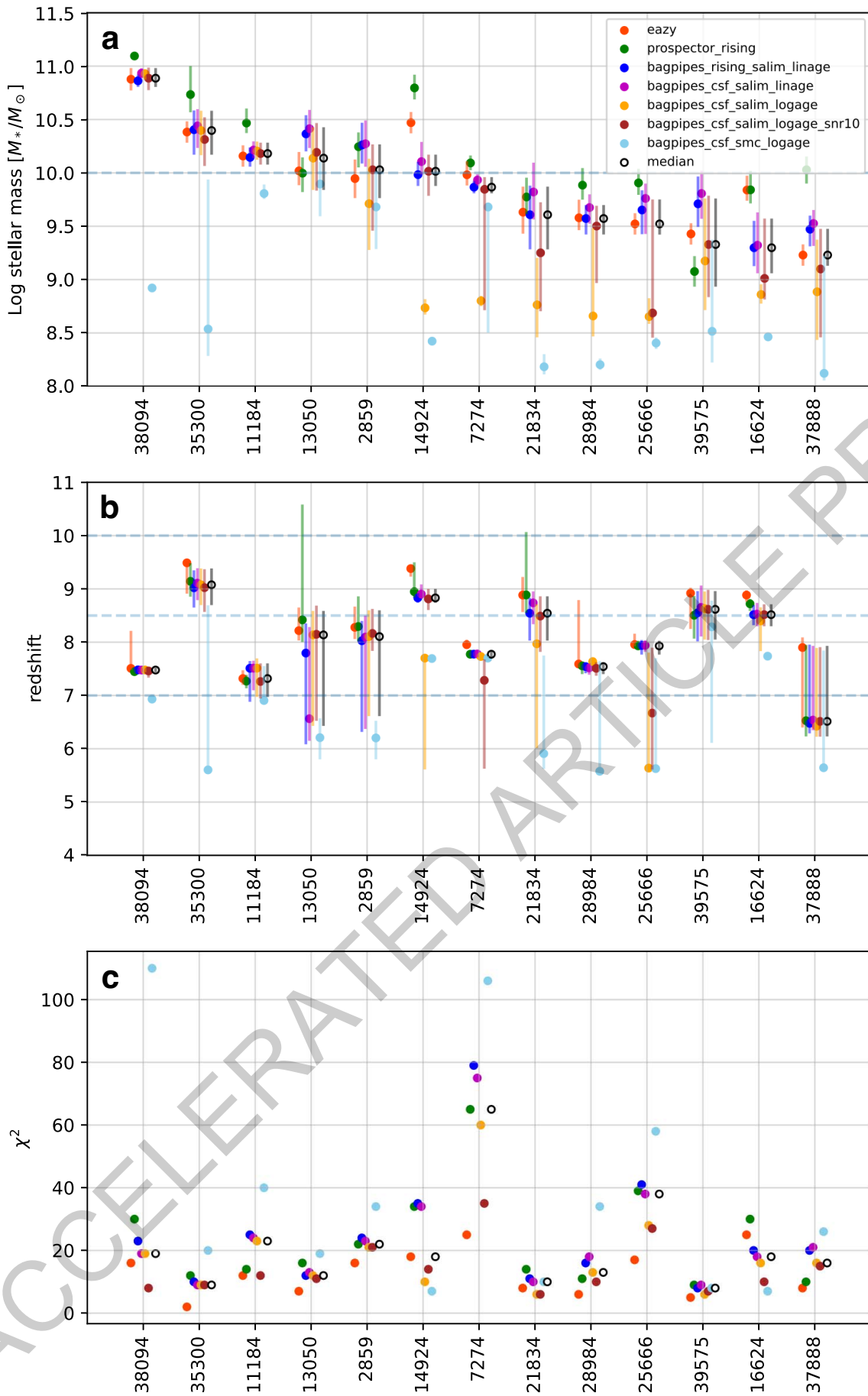


Extended Data Fig. 2

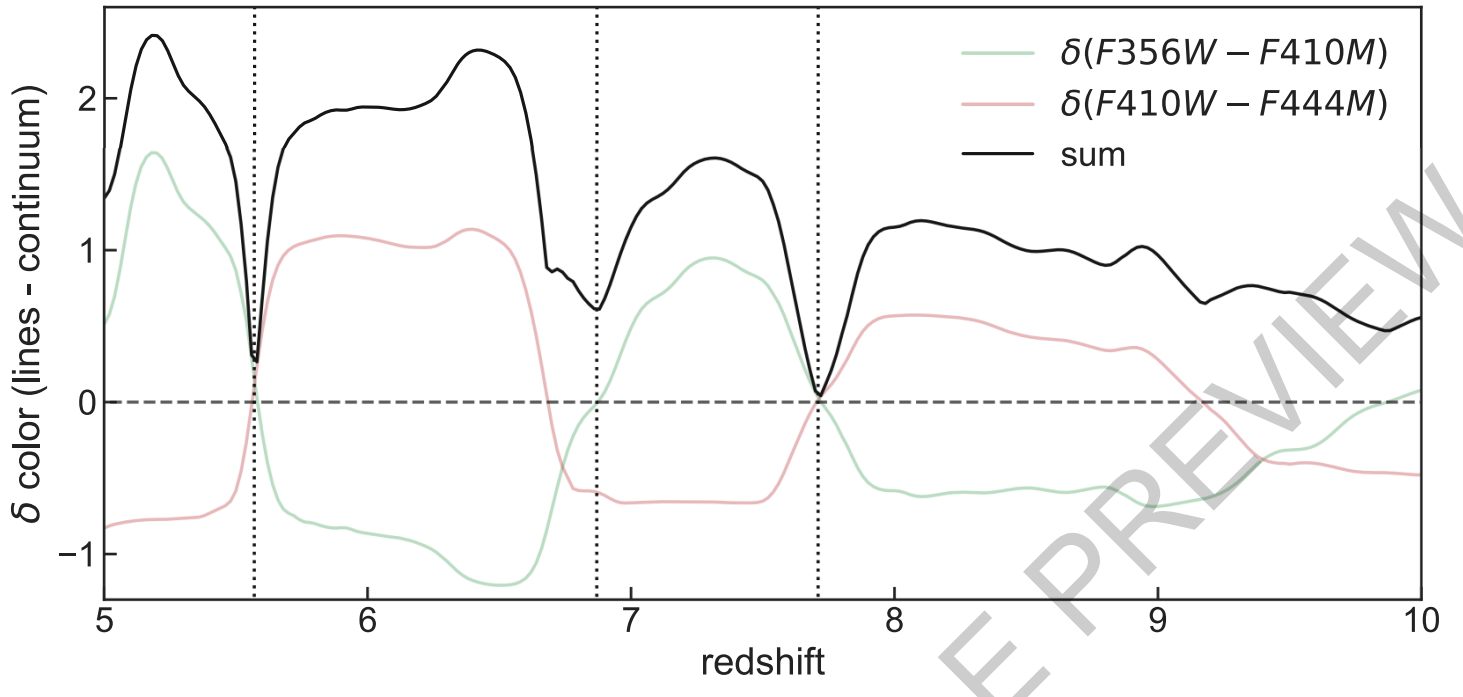
ACCELERATED



Extended Data Fig. 3

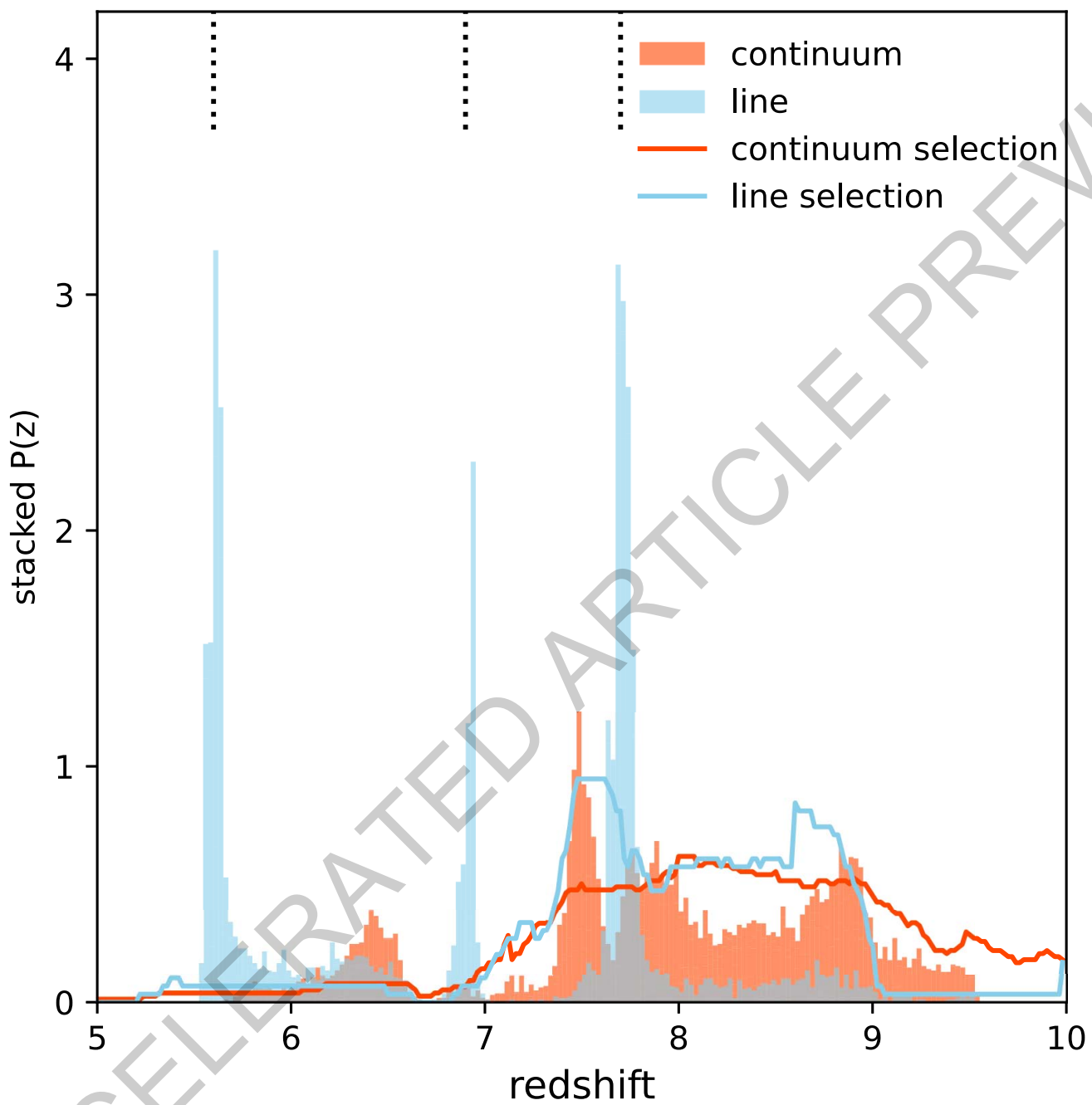


Extended Data Fig. 4



Extended Data Fig. 5

ACCELERATED ARTICLE PREVIEW



Extended Data Fig. 6

id	f435w	f606w	f814w	f115w	f150w	f200w	f277w	f356w	f410m	f444w
2859	3± 4	-2± 4	4± 5	10± 3	15± 4	12± 4	15± 3	52± 2	63± 6	125± 3
7274	-12± 6	1± 4	6± 6	52± 3	47± 4	51± 3	57± 3	138± 2	147± 5	273± 3
11184	-10± 6	-4± 3	-2± 5	37± 4	47± 4	54± 6	74± 3	219± 2	209± 6	225± 3
13050	5± 8	-2± 4	7± 7	10± 3	13± 5	12± 4	23± 3	65± 2	82± 6	148± 4
14924	–	-3± 4	1± 5	10± 3	34± 4	35± 3	46± 2	63± 2	117± 5	183± 2
16624	–	1± 4	-3± 7	22± 4	63± 5	57± 4	75± 3	89± 2	117± 7	212± 3
21834	3± 4	-1± 4	2± 6	4± 3	14± 4	17± 3	18± 2	33± 2	45± 5	83± 3
25666	-5± 7	2± 3	10± 7	24± 3	24± 4	31± 3	34± 3	94± 2	82± 6	163± 3
28984	-3± 7	2± 4	-1± 7	16± 3	22± 4	24± 3	24± 2	55± 2	105± 5	107± 3
35300	–	-4± 3	4± 5	1± 3	15± 4	13± 4	18± 2	38± 2	72± 7	90± 3
37888	1± 5	-4± 3	2± 6	21± 4	17± 4	21± 4	26± 3	59± 2	49± 6	89± 3
38094	2± 4	2± 4	-6± 5	52± 3	86± 4	110± 3	169± 3	546± 3	1003± 8	893± 4
39575	3± 8	4± 6	-6± 11	0± 6	33± 8	25± 8	28± 4	53± 4	53± 11	94± 6

Extended Data Table 1

ACCELERATED ARTICLE PREVIEW

id	ra	dec	redshift	stellar mass $\log(M_*/M_\odot)$
2859	214.840534	52.817942	8.11(+0.49, -1.49)(+0.75, -2.30)	10.03(+0.24, -0.27)(+0.46, -0.75)
7274	214.806671	52.837802	7.77(+0.05, -0.06)(+0.27, -2.15)	9.87(+0.09, -0.06)(+0.30, -1.36)
11184	214.892475	52.856892	7.32(+0.28, -0.35)(+0.38, -0.46)	10.18(+0.10, -0.10)(+0.42, -0.43)
13050	214.809155	52.868481	8.14(+0.45, -1.71)(+2.45, -2.33)	10.14(+0.29, -0.30)(+0.45, -0.54)
14924	214.876150	52.880833	8.83(+0.17, -0.09)(+0.67, -3.22)	10.02(+0.16, -0.14)(+0.90, -1.63)
16624	214.844772	52.892108	8.52(+0.19, -0.22)(+0.46, -0.80)	9.30(+0.27, -0.24)(+0.72, -0.87)
21834	214.902227	52.939370	8.54(+0.32, -0.51)(+1.52, -2.92)	9.61(+0.26, -0.32)(+0.49, -1.50)
25666	214.956837	52.973153	7.93(+0.09, -0.16)(+0.23, -2.32)	9.52(+0.23, -0.10)(+0.52, -1.17)
28984	215.002843	53.007594	7.54(+0.08, -0.14)(+1.25, -1.98)	9.57(+0.13, -0.15)(+0.47, -1.42)
35300	214.830662	52.887777	9.08(+0.31, -0.38)(+0.40, -3.50)	10.40(+0.19, -0.23)(+0.60, -2.11)
37888	214.912510	52.949435	6.51(+1.42, -0.28)(+1.58, -0.90)	9.23(+0.25, -0.10)(+0.92, -1.17)
38094	214.983019	52.955999	7.48(+0.04, -0.04)(+0.74, -0.56)	10.89(+0.09, -0.08)(+0.22, -1.99)
39575	215.005400	52.996706	8.62(+0.34, -0.57)(+0.45, -2.51)	9.33(+0.43, -0.39)(+0.69, -1.11)

Extended Data Table 2

ACCELERATED ARTICLE PREVIEW